Bounds on the microanalyzer array assumption

Israel J. Vaughn[a], Andrey S. Alenin[a], J. Scott Tyo[a]

[a]University of New South Wales Canberra, ACT, Australia

ABSTRACT

Micropolarizer arrays are occasionally used in partial Stokes, full Stokes, and Mueller matrix polarimeters. When treating modulated polarimeters as linear systems, specific assumptions are made about the Dirac delta functional forms generated in the channel space by micropolarizer arrays. These assumptions are 1) infinitely fine sampling both spatially and temporally and 2) infinite array sizes. When these assumptions are lifted and the physical channel shapes are computed, channel shapes become dependent on both the physical pixel area and shape, as well as the array size. We show that under certain circumstances the Dirac delta function approximation is not valid, and give some bounding terms to compute when the approximation is valid, i.e., which array and pixel sizes must be used for the Dirac delta function approximation to hold. Additionally, we show how the physical channel shape changes as a function of array and pixel size, for a conventional $0°, 45°, -45°, 90°$ superpixel micropolarizer array configuration.

Keywords: polarimetry, modulated polarimetry, linear systems, microanalyzer array, micropolarizer array, polarimetric channels

1. INTRODUCTION

Recent developments in the polarimetric system community have resulted in the utilization of linear systems theory to describe polarimetric systems in a general way.[1–11] Most current use of the linear systems formalism for polarimetric instruments involves the assumption of periodic carriers, resulting in δ-functions in the *channel*, or Fourier domain. This assumption works well for large micropolarizer (or microanalyzer) arrays, however for small array sizes it breaks down. In this communication we derive the physical channel structure for rectangular microanalyzer arrays. We show that the physical channel structure is a function of the pixel shape and size and the array size. The physical constraints of the rectangular grid impart a sum of shifted approximate δ-functions multiplied by the Fourier transform of the pixel shape.

The article is organized as follows: In Section 2 the physical form of a single pixel is analyzed in the Fourier (channel) domain for a pixel of arbitrary shape. In Section 3 this physical form is then combined into a finite array which reveals the structure and demonstrates that the physical channel structure is a function of easily manipulated parameters. Section 4 demonstrates a Stokes polarimeter example.

2. PHYSICAL DESCRIPTION

The microanalyzer array will usually adhere to the typical rectangular pixel grid focal plane array (FPA) geometry. Other pixel grid geometries, e.g. hexagonal grids, have been shown to be more efficient in terms of bandwidth,[12] however there are currently no commercially available FPAs known to the authors which offer a hexagonal grid. In this section we derive a *ideal* physical model of the channel structure given the assumptions: 1) spatial integrations are disjoint, 2) Stokes analyzer parameters are constant over each micropolarizer array element except for attenuation, 3) temporal integration is not accounted for, and 4) the pixel array is a regular rectangular grid. The primary physical parameters which affect the channel structure are the analyzer/pixel shape, the analyzer spatial functions, and the array size.

Send correspondence to IJV
IJV: israel.vaughn@gmail.com

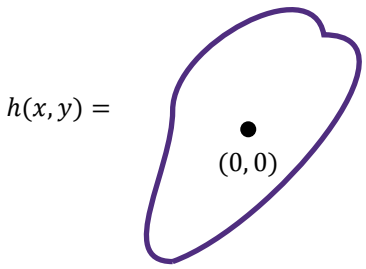

Figure 1: Arbitrary pixel shape represented by the function $h(x,y)$. Notice that it is centered on $(0,0)$.

2.1 Single pixel

We make the assumption here that each pixel has the same shape and attenuation function, and that the each pixel shape is compact and restricted to the pixel pitch size. This function can be represented by $h(x,y)$ as shown in Fig. 1. A single pixel on the rectangular grid can be represented by $h(x-x_i, y-y_j)$ multiplied by the sum of periodic spatial analyzer functions

$$1 + a_1(x,y) + a_2(x,y) + a_3(x,y) \tag{1}$$

at the points (x_i, y_j). A single element at (x_i, y_j) is then measured as

$$\int_{\mathbb{R}^2} \left[s_0(x,y) + a_1(x_i,y_j)s_1(x,y) + a_2(x_i,y_j)s_2(x,y) + a_3(x_i,y_j)s_3(x,y)\right] h(x-x_i, y-y_j)dxdy. \tag{2}$$

where s_0, s_1, s_2, s_3 are the Stokes parameters under measurement.

The system description is then

$$\int_{\mathbb{R}^2} \left[1 + a_1(x_i,y_j) + a_2(x_i,y_j) + a_3(x_i,y_j)\right] h(x-x_i, y-y_j)dxdy. \tag{3}$$

The integration is due to detector integration (spatially, recall that we are ignoring the temporal integration here), which implies that the physical structure in the spatial domain is approximately

$$\begin{aligned} &h(x-x_i, y-y_j) + a_1(x_i,y_j)h(x-x_i, y-y_j) \\ &+a_2(x_i,y_j)h(x-x_i, y-y_j) + a_3(x_i,y_j)h(x-x_i, y-y_j) \end{aligned} \tag{4}$$

Taking the $2-D$ Fourier transform of Eq. (4) results in

$$e^{-2\pi i(x_i\xi + y_j\eta)} H(\xi,\eta)\left[1 + a_1(x_i,y_j) + a_2(x_i,y_j) + a_3(x_i,y_j)\right] \tag{5}$$

where $x \to \xi, y \to \eta$. The $a_i(x_i,y_j)$s corresponding to the microanalyzer elements in Eq. (5) are constants with respect to the Fourier transform, however they are samples of some periodic function(s).

3. ARRAY OF PIXELS

The assumption that $h(x,y)$ is compact (in a mathematical sense) within a bounding rectangle defined by the pixel pitch implies that we can add all of the pixels together. Formally,

$$\begin{aligned} \sum_i \sum_j \Big[&h(x-x_i, y-y_j) + a_1(x_i,y_j)h(x-x_i, y-y_j) \\ &+ a_2(x_i,y_j)h(x-x_i, y-y_j) + a_3(x_i,y_j)h(x-x_i, y-y_j)\Big], \end{aligned} \tag{6}$$

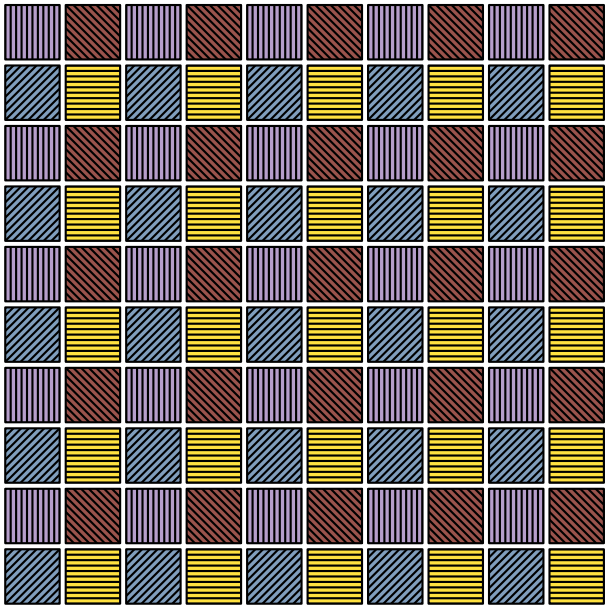

Figure 2: An example of sub-sum selection from a typical linear micropolarizer array. Each element type is periodic over the array. The colors denote the constant multiplier, $a_k(0,0)$ through $a_k(1,1)$, i.e. 4 different periodic sets over the FPA.

gives the physical array response. We can now take the Fourier transform of this sum, and interchange the summation and Fourier transform to obtain

$$\boxed{H(\xi,\eta)\sum_i\sum_j e^{-2\pi i(\xi x_i+\eta y_j)}\Big[1+a_1(x_i,y_j)+a_2(x_i,y_j)+a_3(x_i,y_j)\Big]} \tag{7}$$

We can now change the notation and rewrite Eq. (7) as;

$$\sum_{k=0}^{3} H(\xi,\eta)\sum_{n=-N'}^{N''}\sum_{m=-M'}^{M''} e^{-2\pi i\left(nP_x\xi+mP_y\eta\right)}a_k\left(nP_x,mP_y\right) \tag{8}$$

where n,m describe the pixel numbers, $N'+N'',M'+M''$ represent the number of pixels, and P_x,P_y describe the pixel pitch of the array. The portion of the sum to the right of $H(\xi,\eta)$ represents an approximation of a Fourier series of some function

$$S_k(-\xi,-\eta)=\sum_{n=-\infty}^{\infty}\sum_{m=-\infty}^{\infty} e^{-2\pi i\left(nP_x\xi+mP_y\eta\right)}a_k\left(nP_x,mP_y\right). \tag{9}$$

4. AN EXAMPLE

Commercially available microanalyzer arrays are presently limited to patterns of linear polarizers, typically wire grid polarizers. In this section we use the analysis from Section 2 to present the physical channel shapes for a typical $0°, 45°, 90°, -45°$ superpixel (unit cell) arrangement. In the figures, the channel responses for a_0, a_1, a_2, a_3 are presented separately for clarity. We assume a square pixel shape of side length $9\mu m$.

4.1 Pixel shape

The square pixel shape functions implies that $H(\xi,\eta)$ is proportional to a $\mathrm{sinc}\,(\xi,\eta)$ function, as derived in Section 2. A graph of $H(\xi,\eta)$ is shown in Figure 3. This function is multiplied by the underlying approximate δ-function channel structure which is generated by the sum shown in Eq. (8). The pixel shape has the potential to be used as a kind of filter if subsampling of the microanalyzer array is allowed.

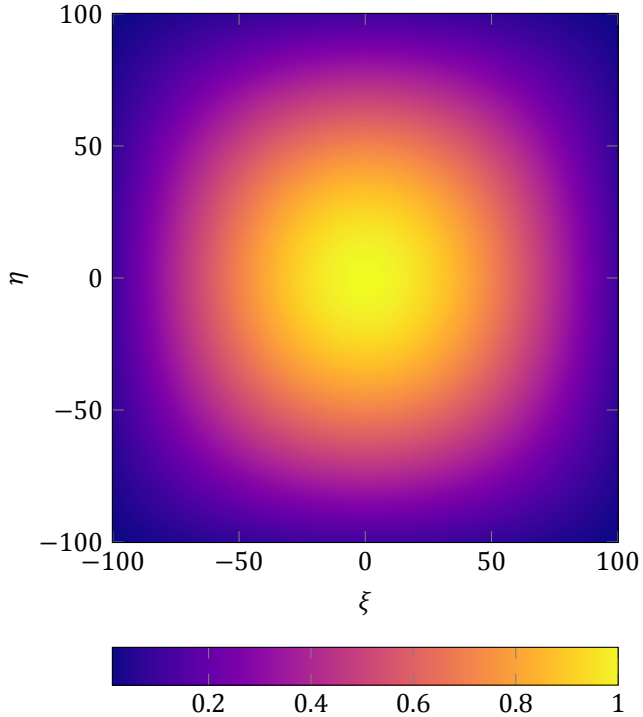

Figure 3: The channel (Fourier) domain result of a square pixel shape function. The axes are in spatial frequency.

4.2 Physical channel structure

The physical channel structure is dependent on four parameters:

- Pixel shape,
- Number of unit cells,
- Unit cell geometry,
- Unit cell analyzer state.

For the specific example shown here, the pixel shape is square, we assume we can vary the number of unit cells, the unit cell geometry is 2×2, and the analyzer states are by

$$a_0(x_i, y_j) = 1 \tag{10}$$

$$a_1(x_i, y_j) = \frac{cos(\pi x_i) + cos(\pi y_j)}{2} \tag{11}$$

$$a_2(x_i, y_j) = \frac{cos(\pi x_i) - cos(\pi y_j)}{2} \tag{12}$$

$$a_3(x_i, y_j) \equiv 0. \tag{13}$$


Figure 4: Conventional unit cell geometry.

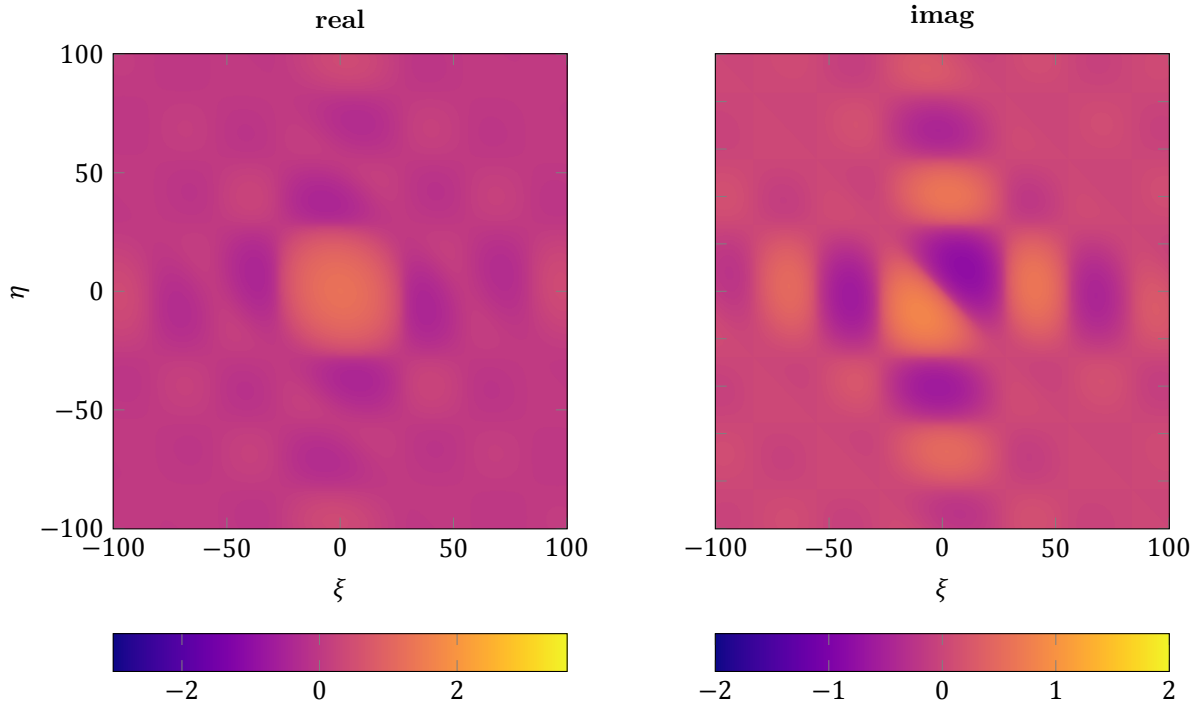

Figure 5: $\mathbf{s}_0$ channel for $N = 2$ unit cells (superpixels). The magnitude is log-modulus transformed.

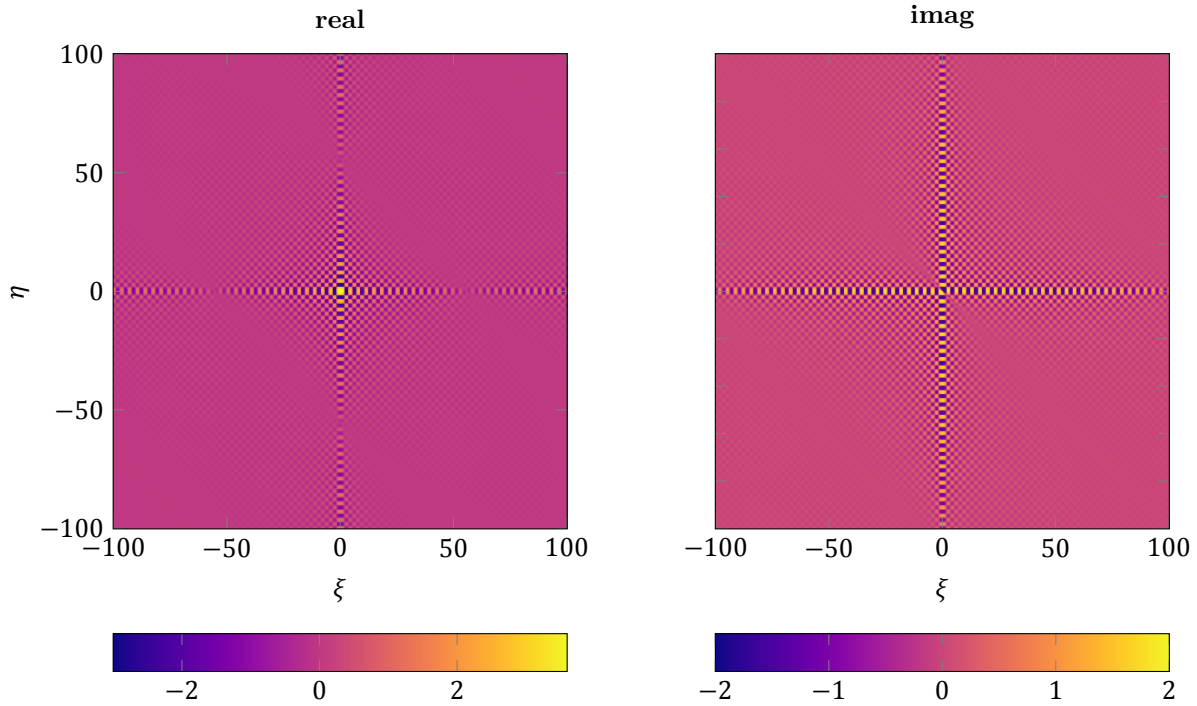

Figure 6: $\mathbf{s}_0$ channel for $N = 32$ unit cells (superpixels). The magnitude is log-modulus transformed.

The unit cell can be defined by the positions $(x_0, y_0) = (0, 0), (x_1, y_0) = (9\mu m, 0), (x_1, y_1) = (9\mu m, 9\mu m), (x_0, y_1) = (0, 9\mu m)$. Equations (11) and (12) imply that the contribution to a_1 and a_2 come from two separate unit cell locations.

The unit cell geometry for the conventional micropolarizer array is fixed, which leaves the number of unit cells

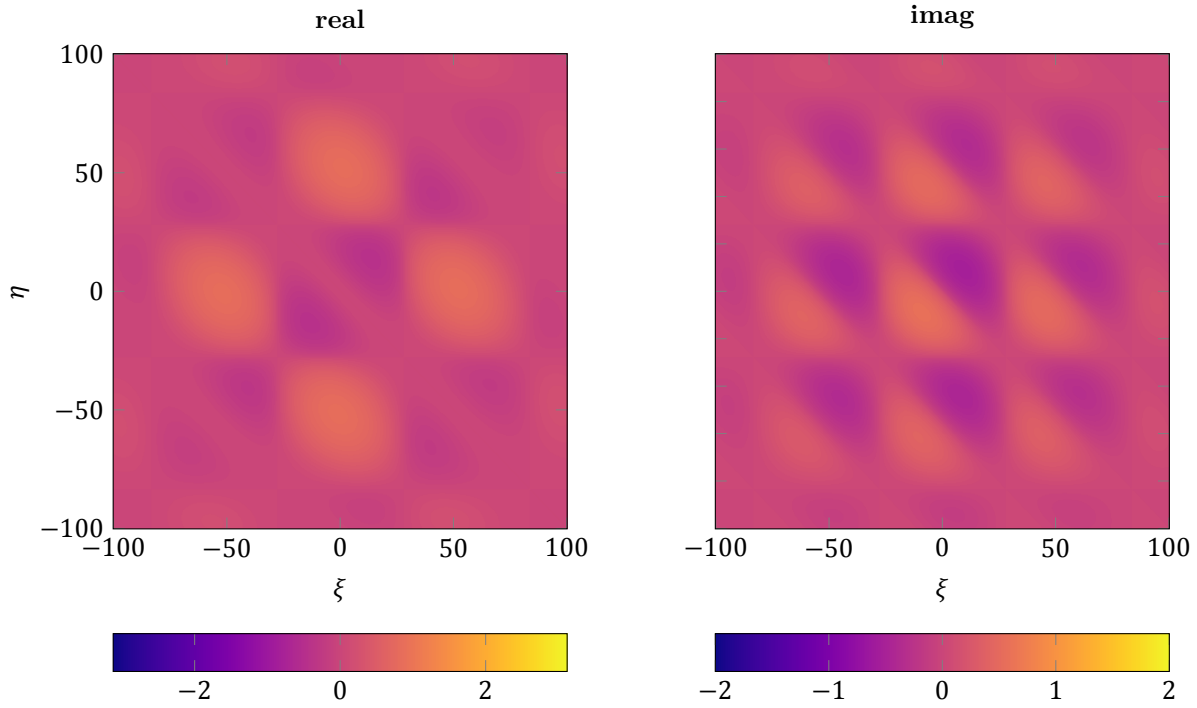

Figure 7: $\mathbf{s}_1$ channel for $N = 2$ unit cells (superpixels). The magnitude is log-modulus transformed.

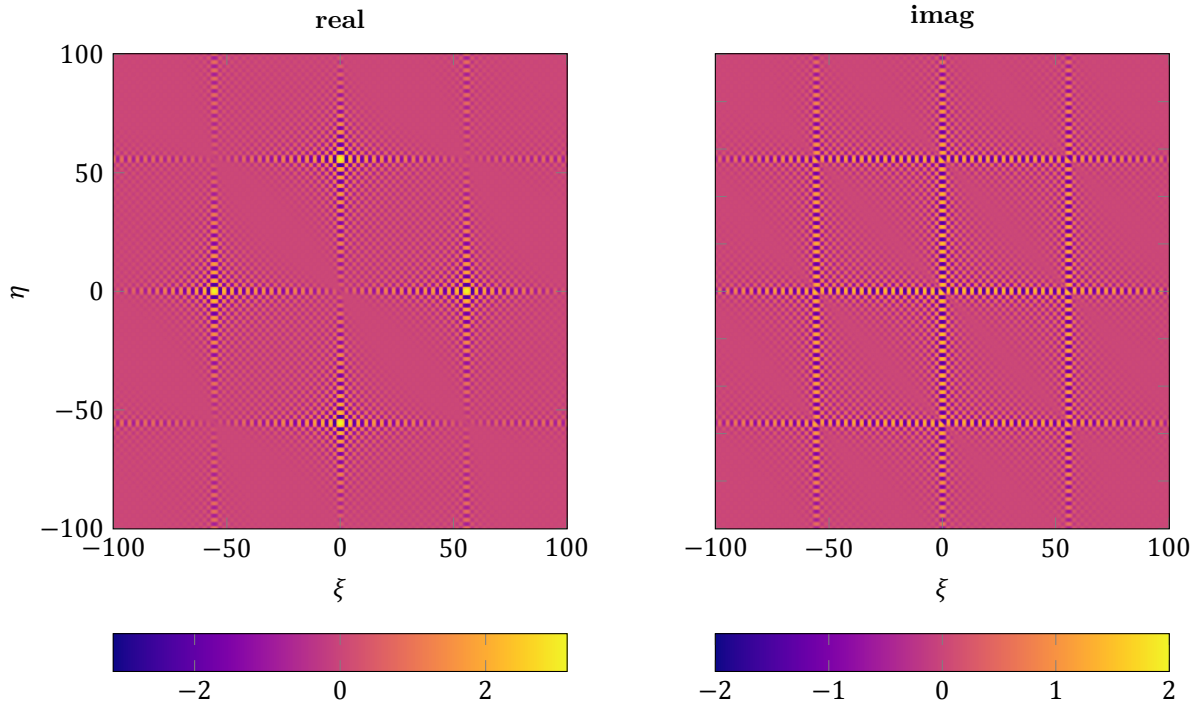

Figure 8: $\mathbf{s}_1$ channel for $N = 32$ unit cells (superpixels). The magnitude is log-modulus transformed.

as a free parameter. The number of unit cells (superpixels) can be different in the x and y directions, however for brevity we assume they are the same, N, here. Equation (8) can then be used to compute the physical channel structure for each of a_0, a_1, a_2 as a function of N.

Figures 5, 7 and 9 show the channel structure of $\mathbf{s}_0, \mathbf{s}_1, \mathbf{s}_2$ for $N = 2$ respectively. Notice that the magnitude is

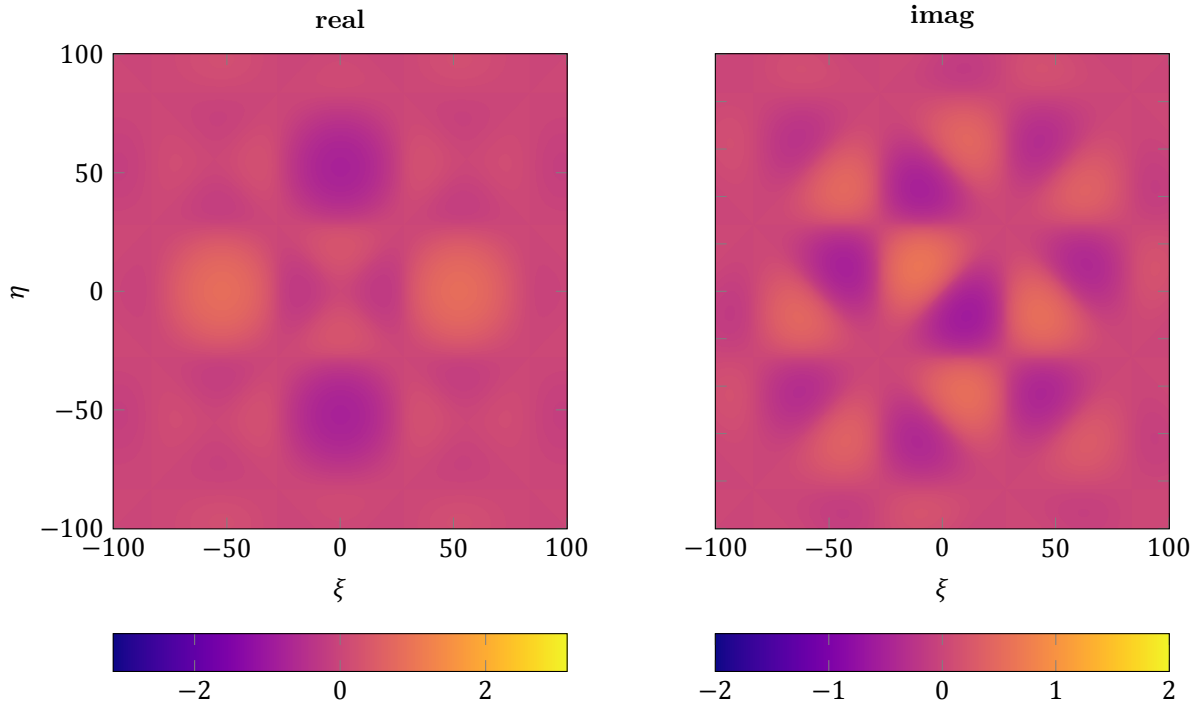

Figure 9: $\mathbf{s}_2$ channel for $N = 2$ unit cells (superpixels). The magnitude is log-modulus transformed.

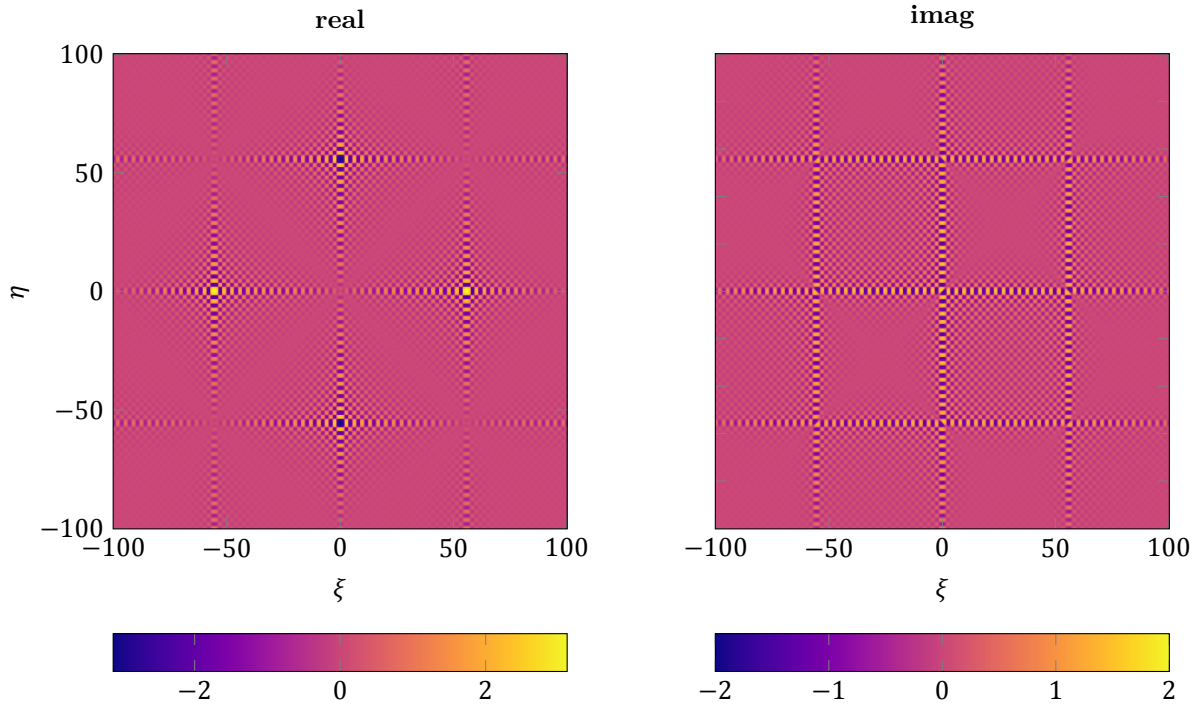

Figure 10: $\mathbf{s}_2$ channel for $N = 32$ unit cells (superpixels). The magnitude is log-modulus transformed.

log-modulus scaled; $y = \text{sgn}(x)\log(|x|+1)$. Figures 6, 8 and 10 show the channel structure of $\mathbf{s}_0, \mathbf{s}_1, \mathbf{s}_2$ for $N = 32$ respectively. The magnitude is also log-modulus scaled. As N increased, the "sharpness" of the approximate δ-functions increases. This sharpness can be used as a specified bound.

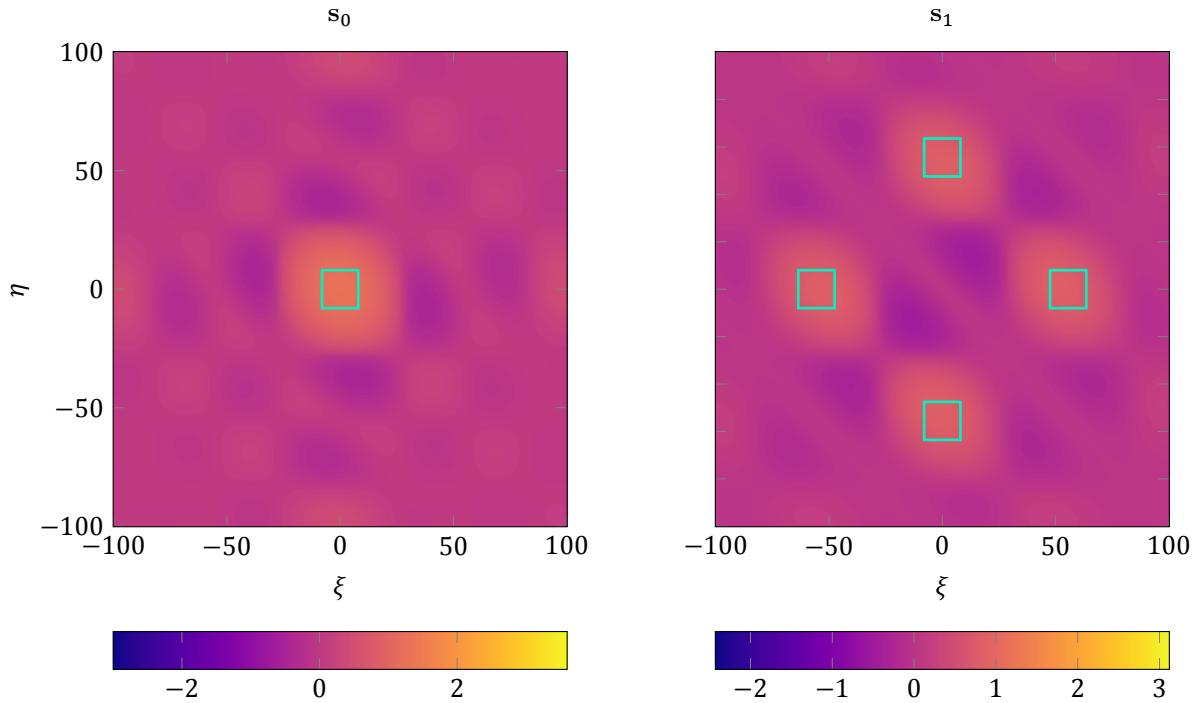

Figure 11: Examples of D_js for $\mathbf{s}_0, \mathbf{s}_1$, left and right respectively, at $N = 2$. These particular D_js are squares with sidelength $16/mm$. $\mathbf{s}_2$ is not shown because the D_js for $\mathbf{s}_2$ are identical to those for $\mathbf{s}_1$.

5. BOUNDS

The analysis in the previous sections provided insight into what occurs to the physical channel structure as the number of unit cells, N, is varied. In this section we briefly analyze how this can be used to derive bounds on N to provide a "sharpness" requirement. First we define a cost function which characterizes the "sharpness."

$$\mathcal{O}(N) = \sum_j \left| \int \int_{D_j} AF_{k,N_x,N_y}(\xi,\eta) d\xi d\eta \right| \tag{14}$$

where

$$AF_{k,N_x,N_y}(\xi,\eta) = H(\xi,\eta) \sum_{n=-N'}^{N''} \sum_{m=-M'}^{M''} e^{-2\pi i\left(nP_x\xi + mP_y\eta\right)} a_k\left(nP_x, mP_y\right), \tag{15}$$

$N', N''; M', M''$ are functions of the number of superpixels in the x, y direction, N_x and N_y respectively, and D_j are two dimensional regions around the relevant δ-function approximations, indexed via j.

D_js characterize specified "sharpness"; $\mathcal{O}(N)$ characterizes how well a given array meets the "sharpness" specification. Figure 11 gives an example of D_js selected for $\mathbf{s}_0, \mathbf{s}_1$. An example of using the cost function to determine N give a "sharpness" requirement follows. If we require that our approximate δ-functions have the main lobe to be within a width of $2/mm$, then we can compute $\mathcal{O}(N)$ for the conventional micropolarizer array as N is varied. The D_js used in this example are squares, as shown in Fig. 11, except that the width has been shortened to $2/mm$. Figure 12 shows the cost function, with a peak at $N = 56$. The cost function decreases for $N > 56$ and then oscillates towards a fixed value. This is due to the integration of the negative side lobes of the approximate δ-functions. $N = 56$ corresponds to the main lobe to side lobe transition just crossing the boundary of the D_js. For this specification, an array with $N = 56$ would be sufficient.

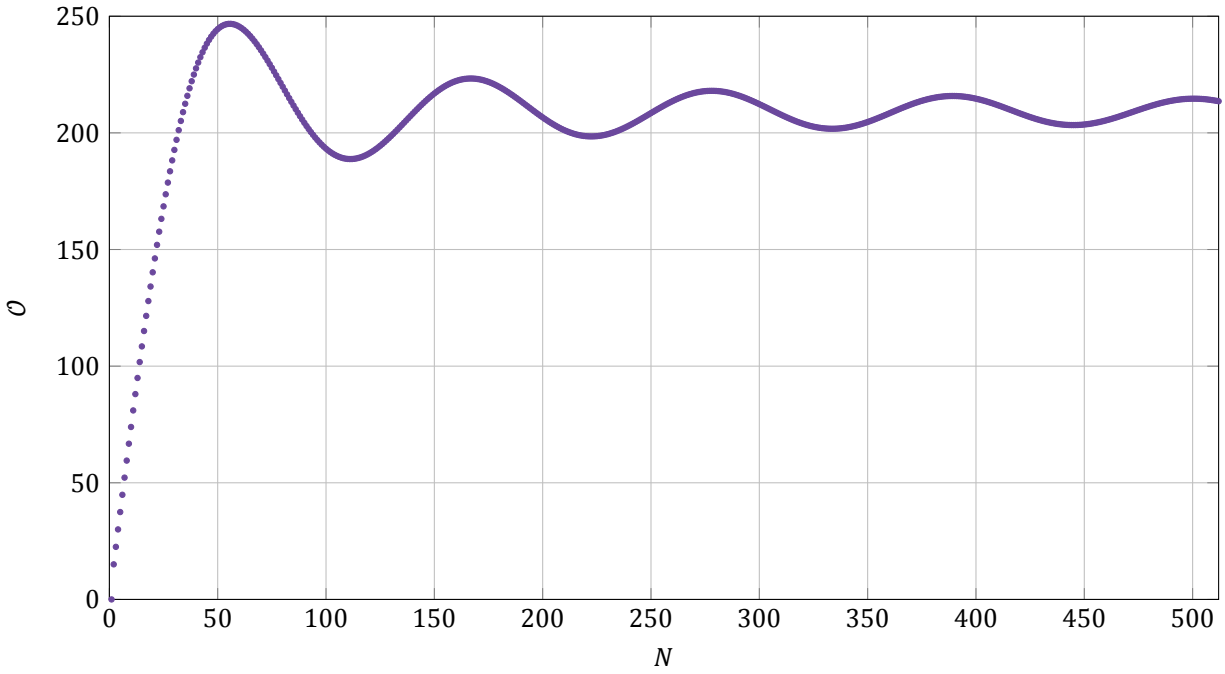

Figure 12: $\mathcal{O}(N)$ as a function of $N = 2, \cdots, 512$. The peak is at $N = 56$.

6. CONCLUSIONS

We have derived a physical channel structure for general microanalyzer arrays in this communication. We have shown that the physical structure depends on the pixel shape, the unit cell geometry, the spatial analyzer layout within the unit cell, and the number of unit cells which are tiled over the detector. This physical structure produces approximate δ-functions. We have shown that when the channel structure is modeled as a set of ideal δ-functions, a certain number of unit cells must be used to meet some specification of "sharpness", or proximity to ideal δ-functions. The "sharpness" is primarily dependent on the number of unit cells used. If sub-sampling is allowed (i.e. more pixels on the underlying focal plane than the overlayed microanalyzer array contains), then this formalism gives potential for pixel shape, spatial bandwidth, and unit cell engineering for specific tasks.

ACKNOWLEDGMENTS

The authors would like to thank Prof. Matthew A. Kupinski for his discussions and questions about micropolarizer arrays.

This work was supported by the Air Force Office of Scientific Research/Asian Office of Aerospace Research and Development under award FA-2386-15-1-4098.

REFERENCES

[1] Oka, K. and Kato, T., "Spectroscopic polarimetry with a channeled spectrum," *Optics Letters* **24**(21), 1475–1477 (1999).

[2] Oka, K., "Singleshot spectroscopic polarimetry using channeled spectrum," *Proc. SPIE* **4919**, 167–175 (2002).

[3] Oka, K. and Kaneko, T., "Compact complete imaging polarimeter using birefringent wedge prisms," *Optics express* **11**(13), 1510–1519 (2003).

[4] Sabatke, D., Locke, A., Dereniak, E. L., Descour, M., Garcia, J., Hamilton, T., and McMillan, R. W., "Snapshot imaging spectropolarimeter," *Optical engineering* **41**(5), 1048–1054 (2002).

[5] Kudenov, M. W., Escuti, M. J., Dereniak, E. L., and Oka, K., "White-light channeled imaging polarimeter using broadband polarization gratings," *Applied optics* **50**(15), 2283–2293 (2011).

[6] Hagen, N. and Kudenov, M. W., "Review of snapshot spectral imaging technologies," *Optical Engineering* **52**(9), 090901–090901 (2013).

[7] LaCasse, C. F., Chipman, R. A., and Tyo, J. S., "Band limited data reconstruction in modulated polarimeters," *Opt. Express* **19**, 14976–14989 (Aug 2011).

[8] LaCasse, C. F., Ririe, T., Chipman, R. A., and Tyo, J. S., "Spatio-temporal modulated polarimetry," *Proc. SPIE* **8160**, 81600K–81600K–11 (2011).

[9] LaCasse, C. F., Tyo, J. S., and Chipman, R. A., "Role of the null space of the drm in the performance of modulated polarimeters," *Optics letters* **37**(6), 1097–1099 (2012).

[10] LeMaster, D. A. and Hirakawa, K., "Improved microgrid arrangement for integrated imaging polarimeters," *Opt. Lett.* **39**, 1811–1814 (Apr 2014).

[11] Alenin, A. S. and Tyo, J. S., "Generalized channeled polarimetry," *J. Opt. Soc. Am. A* **31**, 1013–1022 (May 2014).

[12] Mersereau, R. M., "The processing of hexagonally sampled two-dimensional signals," *Proceedings of the IEEE* **67**(6), 930–949 (1979).